

Broad Electrical Tuning of Graphene-Loaded Plasmonic Antennas

Yu Yao,[†] Mikhail A. Kats,[†] Patrice Genevet,[†] Nanfang Yu,^{†,§} Yi Song,[‡] Jing Kong,[‡] and Federico Capasso^{†,*}

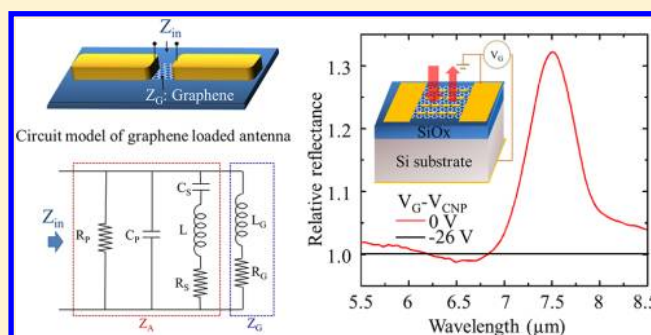
[†]School of Engineering and Applied Sciences, Harvard University, Cambridge, Massachusetts, 02138, United States

[‡]Department of Electrical Engineering and Computer Science, Massachusetts Institute of Technology, Cambridge, 02139, United States

S Supporting Information

ABSTRACT: Plasmonic antennas enable the conversion of light from free space into subwavelength volumes and vice versa, which facilitates the manipulation of light at the nanoscale. Dynamic control of the properties of antennas is desirable for many applications, including biochemical sensors, reconfigurable meta-surfaces and compact optoelectronic devices. The combination of metallic structures and graphene, which has gate-voltage dependent optical properties, is emerging as a possible platform for electrically controlled plasmonic devices. In this paper, we demonstrate in situ control of antennas using graphene as an electrically tunable load in the nanoscale antenna gap. In our experiments, we demonstrate electrical tuning of graphene-loaded antennas over a broad wavelength range of 650 nm ($\sim 140\text{ cm}^{-1}$, $\sim 10\%$ of the resonance frequency) in the mid-infrared (MIR) region. We propose an equivalent circuit model to quantitatively analyze the tuning behavior of graphene-loaded antenna pairs and derive an analytical expression for the tuning range of resonant wavelength. In a separate experiment, we used doubly resonant antenna arrays to achieve MIR optical intensity modulation with maximum modulation depth of more than 30% and bandwidth of 600 nm ($\sim 100\text{ cm}^{-1}$, 8% of the resonance frequency). This study shows that combining graphene with metallic nanostructures provides a route to electrically tunable optical and optoelectronic devices.

KEYWORDS: Reconfigurable antennas, active plasmonics, graphene, nanocircuit loading, antenna array, optical modulator, midinfrared



Plasmonic antennas have enabled applications such as enhancement of light detection^{1,2} and emission,^{3–6} field-enhanced microscopy and spectroscopy,^{7–9} light harvesting,¹⁰ optical data storage,^{11,12} biochemical sensing,^{13,14} nanophotonic integrated circuits,¹⁵ and optical meta-surfaces.^{16–18} While the near- and far-field response of antennas can be tailored by engineering the geometrical parameters, dynamic control of these optical properties is particularly appealing. So far, a number of tuning methods based on thermal,¹⁹ mechanical,²⁰ optical,²¹ and electrical^{22–24} mechanisms have been reported; however, these methods have been limited by slow switching speed^{19,20,22,23} or small tuning ranges.^{21,24} Recently, the possibility of engineering the antenna resonances with “nanocircuit” loads has been proposed theoretically^{25,26} and demonstrated experimentally.^{27,28} Active tuning has been proposed with photoconductive loads,²⁹ but electrically tuning of antenna loads remains elusive. Graphene, a monolayer of hexagonally arranged carbon atoms,³⁰ exhibits gate-voltage dependent optical conductivity and can be used as an electrically tunable plasmonic material.^{31–36} Electrically controllable plasmonic resonances of metallic structures on graphene have been shown at near-infrared (NIR)²⁴ and mid-

infrared (MIR)³⁷ wavelengths, but with very limited tuning ranges (up to 2% of the resonance frequency)²⁴ and small modulation depths (up to 10%).³⁷

In this letter, we demonstrate that graphene can be integrated into the nanogaps of coupled plasmonic antennas to achieve broad tuning of antenna resonance. An effective circuit model is proposed to analyze the effect of the graphene load on a dipole antenna resonance and yield an in-depth understanding of the tuning mechanism. We demonstrate antenna structures with a resonance wavelength tuning range of 650 nm ($\sim 140\text{ cm}^{-1}$, 10% of antenna resonance frequency) in the MIR wavelength region. Additionally, using doubly resonant antenna arrays, MIR intensity modulation is achieved with maximum modulation depth of more than 30% and a bandwidth of 600 nm ($\sim 100\text{ cm}^{-1}$, 8% of the peak frequency).

Theoretical Modeling. The origin of gate-voltage dependent optical properties in graphene lies in the fact that its carrier density and Fermi level can be controlled by the gate voltage, or

Received: December 30, 2012

Revised: February 13, 2013

Published: February 26, 2013

in other words, electrostatic doping. The graphene sheet optical conductivity used in our calculations and simulations is derived within the random-phase approximation (RPA) in the local limit.^{38,39}

$$\sigma_s(\omega) = \frac{i2e^2k_B T}{\pi\hbar^2(\omega + i\tau^{-1})} \ln \left[2 \cosh \left(\frac{E_F}{2k_B T} \right) \right] + \frac{e^2}{4\hbar} \left[\frac{1}{2} + \frac{1}{\pi} \arctan \left(\frac{\hbar\omega - 2E_F}{2k_B T} \right) - \frac{i}{2\pi} \ln \frac{(\hbar\omega + 2E_F)^2}{(\hbar\omega - 2E_F)^2 + 4(k_B T)^2} \right] \quad (1)$$

Here k_B is the Boltzmann constant, T is the temperature, ω is the frequency, τ is the carrier relaxation lifetime, and E_F is the Fermi level, which is dependent on the graphene charge carrier concentration. In our calculation, the carrier relaxation time τ is estimated based on transport measurements on the graphene sample (see Supporting Information, section III, for details) used in our experiment. The first term of eq 1 is attributed to intraband transitions and the second term to interband transitions. When the Fermi level is below half of the photon energy ($E_{ph} = \hbar\omega$), the contribution from the interband transition dominates the optical conductivity. Once the Fermi level is increased above half of the photon energy, interband transitions are diminished due to Pauli blocking and intraband transitions play an important role. In this region, the real part of graphene permittivity ϵ_r (in-plane component, $\epsilon_{\parallel} \triangleq \epsilon_r + i\epsilon_i = 1 + i\sigma_s/\omega\epsilon_0 t_G$; see Supporting Information, section IV, for its calculation) becomes dominant over the imaginary part ϵ_i , as shown in Figure 1. As the charge carrier concentration

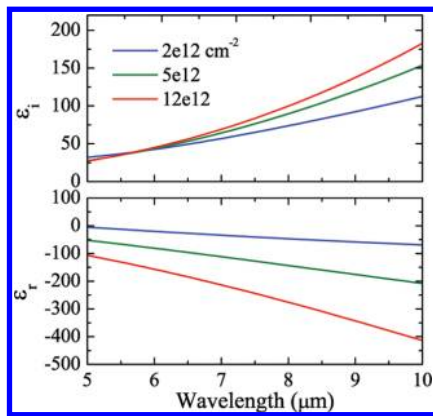


Figure 1. Real (ϵ_r) and imaginary (ϵ_i) parts of the graphene permittivity calculated with RPA at temperature $T = 300$ K for different carrier concentrations in single layer graphene. The mobility is assumed to be $\mu \approx 2,000$ cm²/(V s).

increases, the real part of the permittivity decreases; in the following, we utilize this carrier-concentration-dependent permittivity to tune the resonances of plasmonic antennas.

When a tunable material such as graphene is introduced in the vicinity of an antenna, the effect of the electrostatic doping of the graphene on the antenna resonance frequency ω can be estimated using perturbation theory $(\Delta\omega/\omega) = -(\int \int \int \Delta\epsilon |\mathbf{E}|^2 d\mathbf{r}^3 / 2 \int \int \int \epsilon |\mathbf{E}|^2 d\mathbf{r}^3)$, where $\Delta\epsilon$ is the change in permittivity.⁴⁰ As the graphene charge carrier concentration increases, the real part of the permittivity of the graphene becomes smaller ($\Delta\epsilon < 0$); therefore, the antenna resonance will be blue-

shifted ($\Delta\omega > 0$). To gain physical insight into the tuning mechanism, we developed a circuit model to quantitatively analyze the tuning behavior, which is useful for design and optimization of electrically tunable plasmonic antennas.

We begin by considering an antenna pair with a graphene sheet positioned in the nanogap, as sketched in Figure 2a. The antenna input impedance Z_A , defined as the ratio of the photo-voltage across the gap to the total induced optical displacement current,²⁶ can be represented with an effective circuit model (see Supporting Information, section V, for details), as shown in Figure 2b. The input impedance Z_A calculated by the effective circuit model and the optical cross sections obtained by finite-difference time-domain simulations (FDTD) for the same antenna pair are plotted in Figure 2c. According to antenna theory, the resistance R_A (the real part of Z_A) represents the energy loss due to the antenna, either by scattering, or by internal dissipation into heat. Thus the resistance peak around $7.8 \mu\text{m}$ corresponds to the maximum extinction cross-section, which is the sum of scattering and absorption cross sections. Since the scattering cross-section is much larger than the absorption cross-section and thus dominates the extinction cross-section, the scattering resonance frequency of the dipole antenna can be obtained by finding the resistance peak of its circuit model.

When a graphene sheet is located in the nano antenna gap, the graphene load impedance Z_G is in parallel with the antenna impedance Z_A , as illustrated in Figure 2b. If the gap size is much smaller than both the free space wavelength and the graphene plasmon wavelength (~ 100 to 200 nm in the wavelength range close to the antenna resonance, see Figure S3, Supporting Information), the graphene load impedance can be obtained within the quasi-static approximation (see Supporting Information, section IV, for details) as

$$Z_G = \frac{g}{-i\omega\epsilon_{\parallel}\epsilon_0 w t_G} \quad (2)$$

where g is the gap size, ω is the optical frequency, w is the graphene width and t_G is the graphene thickness ($t_G = 0.3$ nm for a monolayer of graphene). The calculated graphene load impedance is shown in Figure 2d. As the charge carrier concentration increases, the load reactance X_G ($Z_G = R_G - iX_G$) decreases. This indicates that the graphene load is a nanoinductor and its inductance ($L_G = X_G/\omega$) drops with increasing charge carrier concentration, as also shown in Figure 2d. The calculated total impedance Z_T ($Z_T^{-1} = Z_A^{-1} + Z_G^{-1}$) is plotted in Figure 2e, which shows that resistance peak wavelength decreases with higher charge carrier concentration. The antenna resonance frequency shift ($\Delta\omega$) due to the existence of graphene can be estimated analytically as

$$\frac{\Delta\omega}{\omega_0} \approx \frac{1}{2\omega_0^4 C_p^2 L_G L} = \frac{1}{2\omega_0^3 C_p^2 X_G L} \quad (3)$$

which is derived using the effective circuit model (see Supporting Information section V, for more details). In eq 3, ω_0 is the antenna resonance frequency without the graphene load; C_p and L represent the capacitance and inductance, respectively, of the antenna pair without graphene load in the effective circuit model. Equation 3 shows that when graphene load reactance is positive, the resonance is blue-shifted. As the graphene charge carrier concentration increases, the graphene inductance decreases, resulting in further blue-shift. Based on the effective circuit model, we obtain the scattering resonance

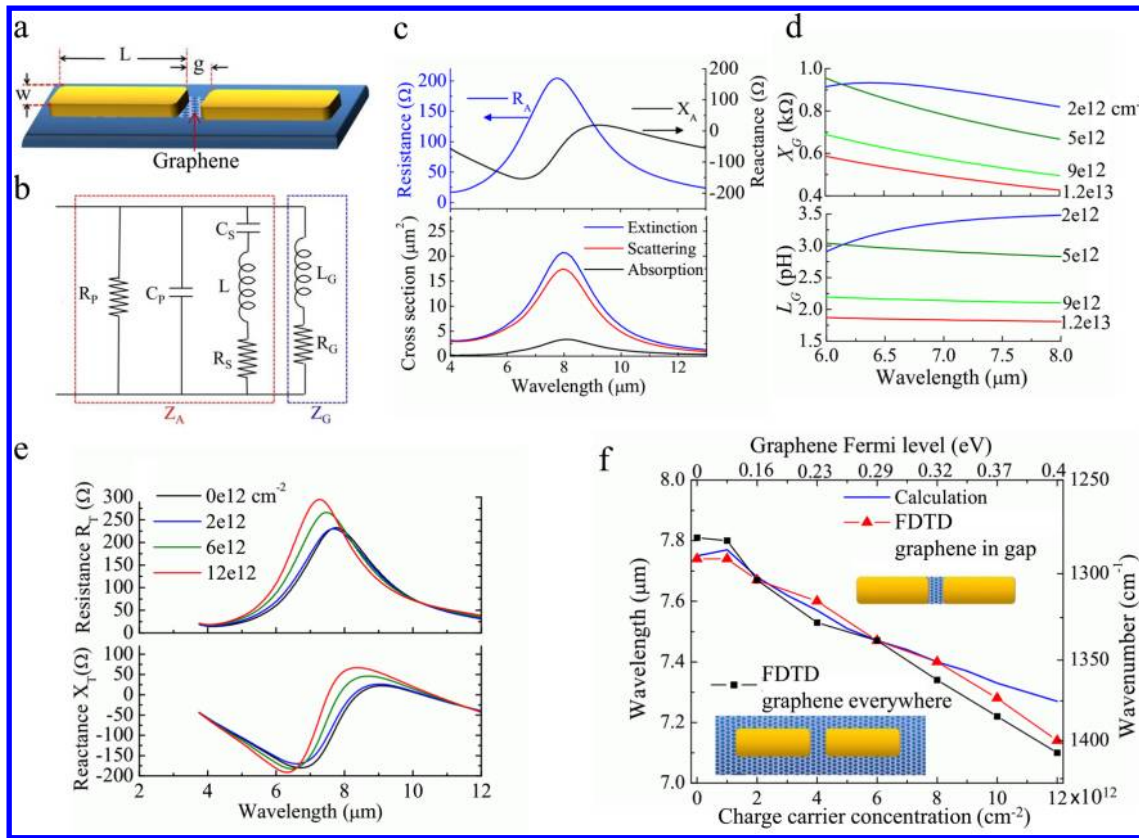


Figure 2. Circuit model for graphene loaded antenna pair. (a) Schematic of an antenna pair, loaded with a graphene sheet in the gap ($g = 20$ nm, $L = 1.84$ μm , $w = 240$ nm). (b) Effective circuit model of the structure in (a). Z_A is the antenna impedance and its effective circuit elements are $R_p = 1.0$ k Ω , $C_p = 3.21\text{E}-17$ F, $C_s = 3.84\text{E}-17$ F, $L = 9.2\text{E}-13$ H, $R_s = 63$ Ω . Z_G is the graphene load impedance; L_G and R_G represent its inductance and resistance, respectively. (c) Input resistance and reactance (real part and imaginary part of the impedance Z_A) of the antenna in part a, and extinction, scattering, and absorption cross sections extracted from FDTD simulations. (d) Reactance (X_G) and inductance (L_G) of the graphene load in antenna nanogap ($g = 20$ nm, $w = 240$ nm). (e) Resistance and reactance (real part and imaginary part of the impedance Z_T) of the graphene loaded dipole antenna for different carrier concentrations. (f) Scattering resonance peaks obtained from the circuit model (solid line: calculation), FDTD simulation (stars: antenna pair with graphene only in the gap; squares: antenna pair on a large graphene sheet) as a function of graphene carrier concentration. The corresponding graphene Fermi levels are given on the top axis beside the major ticks.

peaks of the graphene-loaded antenna pair for different charge carrier concentration, as shown in Figure 2f. The tuning behavior agrees well with the FDTD simulation results of the same structure, also plotted on Figure 2f as the “FDTD graphene in gap”. In both the circuit model and the “FDTD graphene in gap”, we assumed that graphene was only located within the antenna gap. The comparison with FDTD simulation of the same antenna pair on a large, continuous sheet of graphene (“FDTD graphene everywhere” in Figure 1f) indicates that the effect of graphene outside the antenna gap is almost negligible. This is because the light intensity is highly localized within the nanogap, where the light-graphene interaction is greatly enhanced.

We used this circuit model to optimize antenna structures for a wider tuning range of resonant wavelength. It is clear from eq 3 that a smaller inductance of the graphene load L_G leads to a larger frequency shift. From eq 2, we can obtain the expression for graphene load inductance (see Supporting Information, section IV for the derivation).

$$L_G \approx \frac{g}{\omega^2 \epsilon_0 (-\epsilon_r) w t_G} \quad (4)$$

For the same graphene charge carrier concentration, the L_G decreases linearly with the antenna gap size. Thus we expect a wider tuning range as the gap size shrinks. To verify this, we

calculated the tuning ranges based on simulation results for antenna gap sizes from 50 to 10 nm, as shown on Figure 3b. A dramatic increase of the tuning range is observed as the gap size shrinks. From an optical perspective, decreasing gap size g dramatically increases the field intensity within the gap,⁴¹ where the localized field overlaps with the graphene load. Therefore, the tuning range is expected to be proportional to the overlap of field intensity and graphene, (also known as the confinement factor, $\Gamma = \iint_{\Omega} |E|^2 d\mathbf{r}^3 / \iint |E|^2 d\mathbf{r}^3$, the integral in the numerator is calculated over the graphene volume Ω , as illustrated in Figure 3a). From the field distribution obtained by FDTD simulations, we calculated the confinement factors for different gap sizes, as also plotted on Figure 3b. It is clear that the dependence of the tuning range on the gap size is mainly due to the change of the confinement factor.

The tuning range of resonant wavelength can be further increased by coupling multiple antennas end-to-end, as depicted in Figure 3c, since in such a linear array each antenna has both ends loaded by graphene. Figure 3d shows that the wavelength tuning ranges of the near field enhancement in the nanogap center of an antenna pair, an antenna quadrupole and a 1D antenna array (all with the same gap size and antenna dimensions) are 600 nm, 900 and 1100 nm, respectively, which clearly indicates that the tuning range increases as the number of coupled antennas increases. Figure 3d also shows scattering

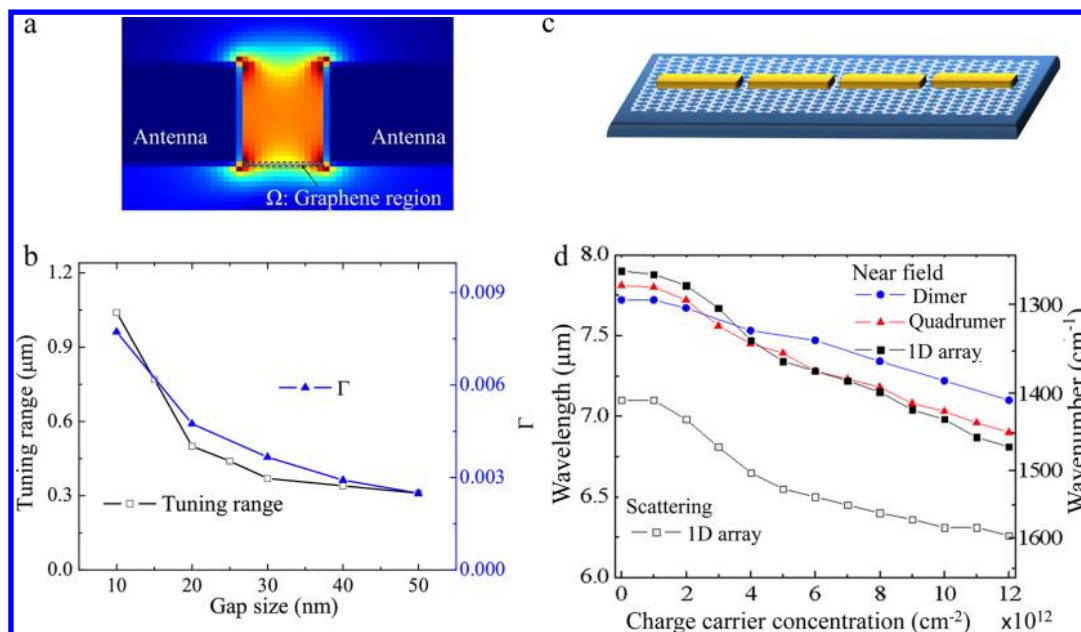


Figure 3. Structure optimization for wide wavelength tuning ranges. (a) Field distribution in the gap between antennas. (b) Calculated tuning ranges and confinement factors Γ , as a function of the gap size g . (c) Schematic of end-to-end coupled antenna array. (d) Near field enhancement (in the center of the gap) peak wavelength of an antenna pair, antenna quadruplet, and 1D antenna array (gap size 20 nm) as well as scattering resonance peak wavelength of 1D antenna array obtained by FDTD simulations (the substrate is 30 nm silicon oxide on p-type doped silicon). All simulations and calculations are performed for 240 nm wide, 1.8 μm long, 40 nm thick gold antennas.

resonance peaks for the 1D antenna array. These peaks are blue-shifted with respect to the near field resonances, which is expected for antennas due to both internal and radiation damping,⁴² and their tuning behavior is consistent with that of the near field enhancement.

Sample Fabrication and Characterization. We fabricated antenna arrays with lateral spacing P_x on a gated graphene layer, as depicted in Figure 4a. A large area graphene sheet grown by atmospheric pressure chemical vapor deposition (CVD) was first transferred onto a 30 nm dry thermal oxide layer on a doped silicon substrate. The antenna structures and metal contact pads were fabricated on the graphene sheet by electron beam lithography (EBL), electron beam evaporation (5 nm Pd and 30 nm Au) and lift-off. Figure 4b shows the scanning electron microscopy (SEM) picture of one device and the zoom-in over a small region. The conductance of such a device is measured by applying voltage between the two contact pads and plotted in Figure 4c as a function of the gate voltage. For the as-fabricated graphene sample, the charge neutral point (CNP, where the numbers of electrons and holes are equal) is reached at $V_G = V_{\text{CNP}} = 0.5$ V, as indicated with a blue arrow on the plot. The gate voltage V_G applied on the samples is limited between -14 and $+14$ V, due to the breakdown electric field of the gate dielectric (~ 0.5 GV/m for silicon oxide). The dynamic range of graphene permittivity achieved is from ~ 0 to -130 (real part ϵ_R) at 7 μm , as shown in Figure 4c. After the graphene is chemically p-doped by immersing it in diluted nitric acid (HNO_3) ($\sim 1\%$),⁴³ the charge neutral point is moved to a much higher voltage, i.e., $V_{\text{CNP}} = 12$ V, as indicated with a red arrow on Figure 4c. Thus the maximum graphene charge carrier concentration achievable is increased from $(5.0\text{--}6.0) \times 10^{16} \text{ m}^{-2}$ to $1.0\text{--}1.1 \times 10^{17} \text{ m}^{-2}$, resulting in over 50% larger dynamic range of graphene permittivity (ϵ_R : from ~ 0 to -200). The frequency response of the gate voltage is measured to determine the modulation

cutoff frequency (~ 40 MHz, see Supporting Information, section VIII, for details), which can be increased by shrinking the size of contact pads and graphene sheet.

Electrically Tunable Antenna Resonance Wavelength.

The reflectance of our samples were measured using a Fourier transform infrared (FTIR) spectrometer connected with a MIR microscope (NA=0.4) (see Figure S7, Supporting Information). The measured reflectance spectra of an antenna array (with a lateral period $P_x = 2.6 \mu\text{m}$) are shown in Figure 4d. The extracted wavelength of the reflectance peak is plotted in Figure 4e as a function of applied voltages ($V_G - V_{\text{CNP}}$) and corresponding graphene charge carrier concentration. The tuning range of the chemically doped sample is increased to 650 nm (140 cm^{-1} , $\sim 10\%$ of the center frequency) from ~ 400 nm before chemical doping. Simulation results for the doped sample are also plotted for comparison. The tuning behavior for graphene charge carrier concentration above $3 \times 10^{12} \text{ cm}^{-2}$ shows good agreement, with an average tuning rate of $\sim 7 \text{ cm}^{-1}/\text{V}$. For lower charge carrier concentrations, the deviation is attributed to the residual conductivity of the graphene sheet which is a consequence of the surface roughness of the substrate and the distribution of defects or ions in graphene,⁴⁴ while in simulations a uniform charge carrier concentration is assumed.

Midinfrared Light Intensity Modulator Based on a Double Resonance Effect. In an antenna array, besides the antenna resonance, the lateral array with period P_x also leads to a grating resonance at a wavelength $\lambda_G = n_{\text{eff}} P_x$.⁴⁵ Our experiments show that when the lateral period P_x in the antenna array decreases to 2 μm while keeping all other parameters the same, the reflection spectra becomes narrower and stronger (see Figure S9, Supporting Information). The reason is that when the grating resonance wavelength is equal to the antenna resonance wavelength ("double resonance"), constructive interference between scattered light from adjacent

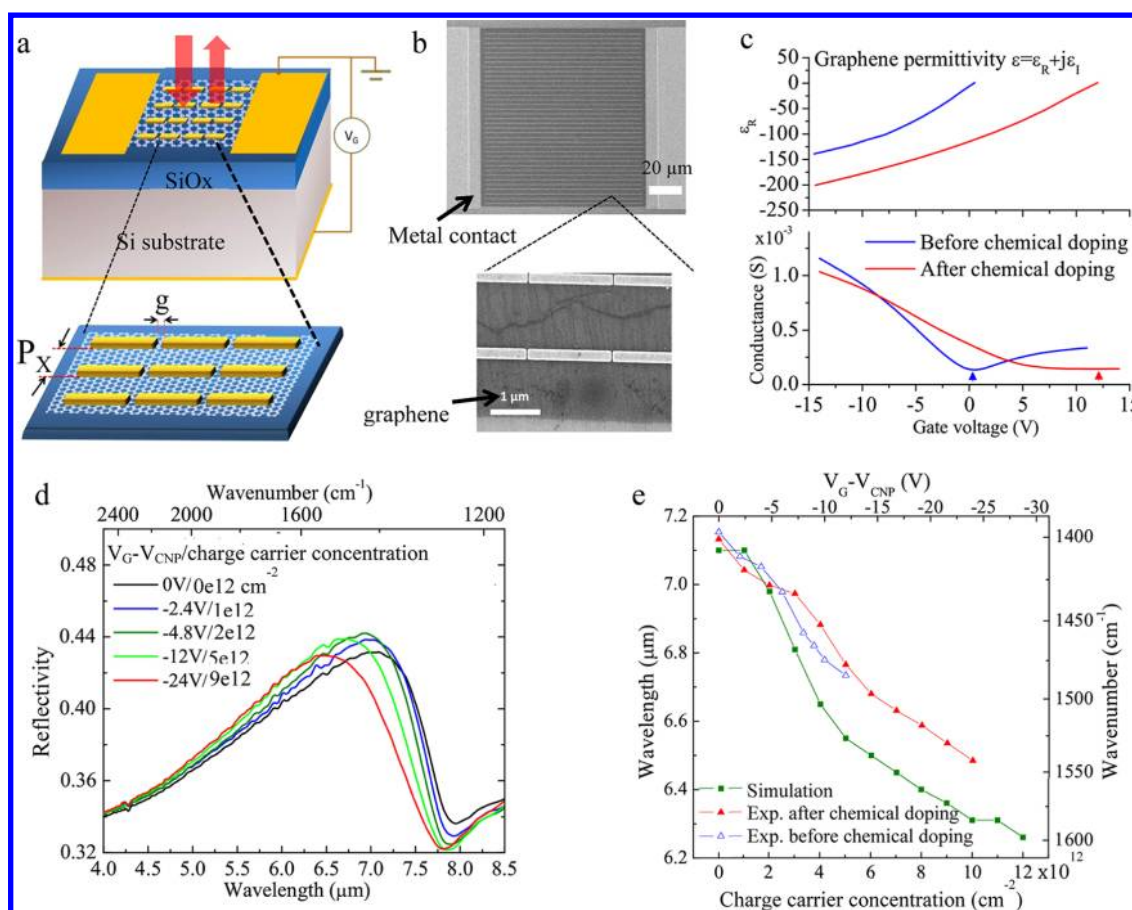


Figure 4. Device configuration and experimental results of antenna array with tunable resonance. (a) Schematic of the tunable plasmonic device with back gate voltage and the antenna array on a gated graphene sheet. (b) Scanning electron microscope (SEM) image of one device and a zoomed-in portion of the antenna array on graphene. (c) Measured graphene conductance (bottom) and calculated graphene permittivity (top) for graphene samples before and after chemical doping as a function of gate voltage. (d) Measured reflection spectra from an antenna array after chemical doping (antenna length 1.8 μm , gap size 20 nm, lateral period 2.6 μm) for different gate voltages V_G (V_{CNP} is the gate voltage at the charge neutral point, where the numbers of holes and electrons in the graphene sheet are equal.) and the corresponding charge carrier concentrations. (e) Simulated (solid red squares) and measured (blue open triangles: before chemical doping, red solid triangles: after chemical doping) reflectance peak wavelengths for the same antenna array as a function of gate voltage and charge carrier concentration.

rows of antennas leads to a higher field enhancement and stronger reflectance peaks.⁴⁵ FDTD simulations of an antenna array with lateral period $P_x = 2 \mu\text{m}$ (Figure 5a) show a strong modulation effect on the reflection intensity as the graphene charge carrier concentration changes. This is because when the antenna resonance is tuned away from the lateral array resonance, the constructive interference is greatly diminished. The measured reflection spectra from such an array are shown in Figure 5b for different gate voltages and the corresponding graphene charge carrier concentrations. The tuning behavior of extracted reflection peaks, as plotted in Figure 5c, shows good agreement with the FDTD simulation results. The measured relative reflectivity spectra for different gate voltages with respect to the reflectivity of the same sample at $V_G - V_{\text{CNP}} = 26.4 \text{ V}$ are shown on Figure 5d. A maximum intensity modulation of $\sim 30\%$ is achieved at wavelength of 7.8 μm , with a 3 dB bandwidth of $\sim 600 \text{ nm}$ ($\sim 100 \text{ cm}^{-1}$, 8% of the center frequency). FDTD simulation results also show that if the sample is used in transmission mode, a larger modulation depth ($\sim 66\%$) can be achieved at 7.7 μm , with the same bandwidth as the reflection mode, as shown in Figure 5, parts e and f, which provides a promising solution for compact, broadband optical modulators in MIR wavelength range.

Conclusion. Despite its atomically small thickness, graphene can be a promising element of tunable plasmonic components, especially in structures with large localized field enhancement. By using graphene as a tunable load in the antenna nanogaps, we achieved dynamic control of the antenna resonances with a large tuning range. An effective circuit model is presented as a simple and powerful tool to predict the tuning behavior. FDTD simulations using the optical conductance of graphene obtained within random phase approximation show good agreement with our experimental results. Modulation of both the spectral position of a resonance and its intensity is demonstrated with antenna arrays in the MIR wavelength range. Resonance tuning ranges over 650 nm (140 cm^{-1} , $\sim 10\%$ of the resonance frequency) and intensity modulation over 30% with a 3 dB bandwidth of 600 nm ($\sim 100 \text{ cm}^{-1}$, 8% of the center frequency) are achieved with different array designs. These results show that graphene is ready to play a unique role for dynamically controllable plasmonic structures, leading to applications such as tunable optical filters/reflectors, modulators, tunable SERS substrates, and reconfigurable metasurfaces. Moreover, in situ control of plasmonic antennas with subwavelength-scale elements makes it possible to

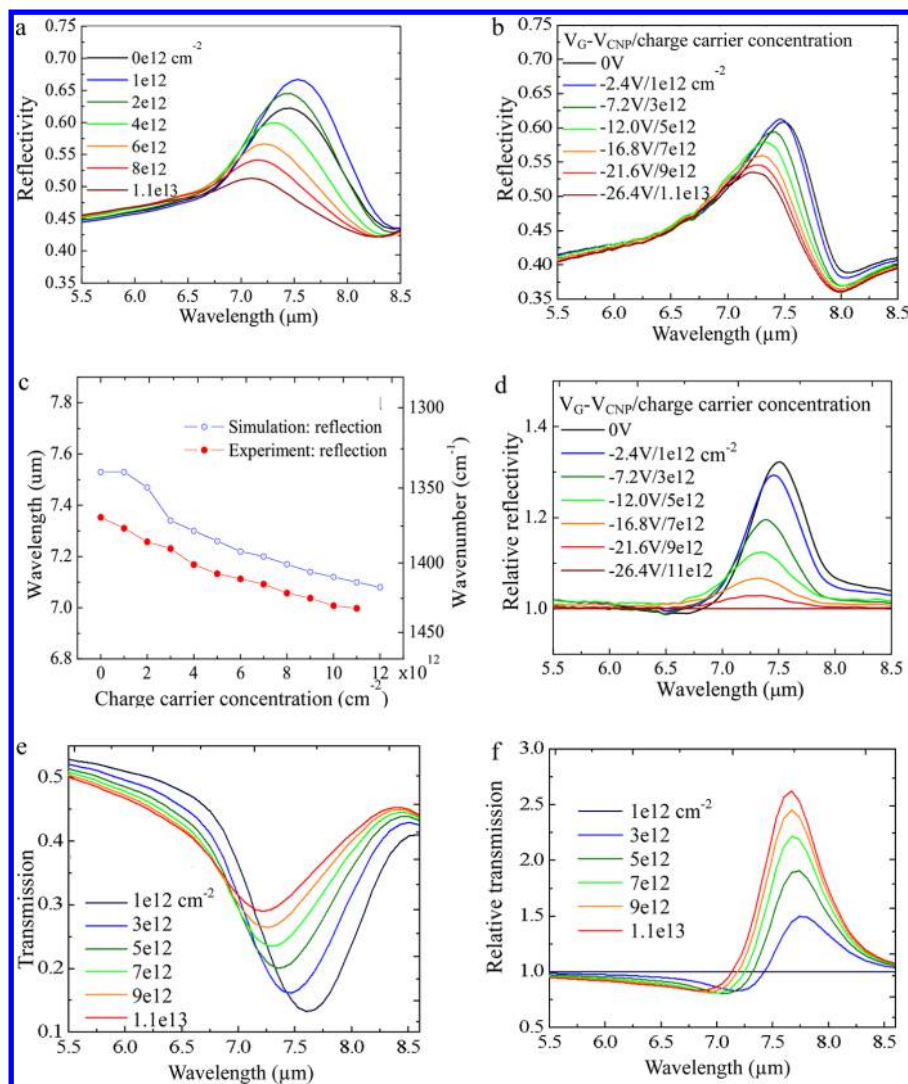


Figure 5. Midinfrared optical intensity modulator based on antenna array with double resonance. (a) Calculated reflection spectra of an antenna array for different charge carrier concentrations obtained by FDTD simulation. (b) Measured reflection spectra for different gate voltages and corresponding charge carrier concentration. (c) Simulated (open blue circles) and measured (solid red circles) reflection peaks as functions of gate voltages (V_G) and graphene charge carrier concentration. (d) Measured relative reflectivity (normalized by that for $V_G - V_{\text{CNP}} = -26.4 \text{ V}$) for different gated voltages and corresponding charge carrier concentration. (e) Calculated transmission spectra and (f) normalized transmission spectra (normalized by that for the carrier concentration of $1 \times 10^{16} \text{ m}^{-2}$) for different charge carrier concentrations obtained by FDTD simulation. All the simulation and experiment results are obtained from an array with antennas $1.8 \mu\text{m}$ long, 240 nm wide, gap size 20 nm and lateral period $P_x = 2.0 \mu\text{m}$.

electrically manipulate light at the nanoscale, which may lead to highly compact photonic and optoelectronic devices.

Methods. Modeling and Simulation. We used the time domain solver of CST microwave studio (<http://www.cst.com>) to calculate the antenna impedance in Figure 1. The total simulation volume surrounding the antenna has an assumed permittivity of 1.7. The same setting is used for the Lumerical FDTD simulation (<http://www.lumerical.com/>).

In the FDTD simulations, the graphene layer is modeled as an anisotropic material with in-plane permittivity ϵ_{\parallel} and out of plane permittivity ϵ_{\perp} . The former is calculated from the graphene sheet optical conductivity and the latter is assumed to be 2.5 .⁴⁶ The scattering, absorption and extinction cross sections are calculated using a total-field/scattered-field source. The near-field enhancement is obtained in the center of the antenna nanogap at a height of 40 nm above the substrate surface. For the simulations in Figure 3 and Figure 4, the

antennas are placed on 30 nm SiO_2 on silicon substrate. All parameters are chosen to be the same as the fabricated structures.

Fabrication Process for the Voltage Tunable Antenna Structures on Graphene. The antenna arrays on gated graphene are fabricated on 30 nm dry thermal oxide layer on a doped silicon substrate. After patterning the antenna arrays and metal contacts on the graphene, unnecessary graphene was removed by photolithography and oxygen plasma. For probing and bonding purposes, Ti/Au ($20 \text{ nm}/300 \text{ nm}$) pads are evaporated on the oxide layer where graphene is removed to provide good adhesion. Then gate contact (Ti/Au: $20 \text{ nm}/300 \text{ nm}$) is evaporated on the backside of the silicon substrate. The chemical doping of graphene is achieved by immersing the fabricated sample in diluted nitric acid (HNO_3 , 1%) for 5 min and by drying with nitrogen gas.

Optical and Electrical Measurements. The reflectance spectra were measured using a FTIR connected with a MIR microscope. Spectral measurements were taken from an $80\ \mu\text{m} \times 100\ \mu\text{m}$ aperture. As a reference, the reflectance spectrum from a 300 nm thick gold film on the same substrate (30 nm silicon oxide on silicon substrate) is also measured. The frequency resolution is $2\ \text{cm}^{-1}$ and every spectrum is averaged over 100 scans. The conductance of graphene samples are measured using a parametric analyzer (Agilent 4156C) with varying gate voltages. An integration time of 1 s is chosen for each data point.

■ ASSOCIATED CONTENT

Supporting Information

Calculations of graphene plasmons, carrier relaxation time of our CVD graphene sample and graphene load impedance; equivalent circuit model analysis of graphene loaded antenna pair; experimental details of graphene growth and transfer, and reflectance spectra measurement and modulation speed of gated graphene with antenna array. This material is available free of charge via the Internet at <http://pubs.acs.org>.

■ AUTHOR INFORMATION

Corresponding Author

*E-mail: capasso@seas.harvard.edu. Telephone: 1-617-384-7611. Mailing address: Pierce 205A, 29 Oxford Street, Cambridge, MA 02138.

Present Address

[§]Department of Applied Physics and Applied Mathematics, Columbia University, New York, NY 10027.

Notes

The authors declare no competing financial interest.

■ ACKNOWLEDGMENTS

We gratefully acknowledge discussions with M. Allen, R. Blanchard, Y. Dan, C. Wang, Y. Zhang. Device fabrication was performed at the Center for Nanoscale Systems, which is a member of the National Nanotechnology Infrastructure Network supported by the National Science Foundation (NSF). This research is supported by NSF (ECCS-1230477). M.A.K. is supported by the NSF via a graduate research fellowship.

■ REFERENCES

- (1) Tang, L.; Kocabas, S. E.; Latif, S.; Okay, A. K.; Ly-Gagnon, D. S.; Saraswat, K. C.; Miller, D. A. B. *Nat Photonics* **2008**, *2*, 226–229.
- (2) Cao, L. Y.; Park, J. S.; Fan, P. Y.; Clemens, B.; Brongersma, M. L. *Nano Lett* **2010**, *10*, 1229–1233.
- (3) Cubukcu, E.; Kort, E. A.; Crozier, K. B.; Capasso, F. *Appl. Phys. Lett.* **2006**, *89*, 093120.
- (4) Yu, N.; Cubukcu, E.; Diehl, L.; Belkin, M. A.; Crozier, K. B.; Capasso, F.; Bour, D.; Corzine, S.; Hofler, G. *Appl. Phys. Lett.* **2007**, *91*, 173113.
- (5) Farahani, J. N.; Pohl, D. W.; Eisler, H. J.; Hecht, B. *Phys. Rev. Lett.* **2005**, *95*, 017402.
- (6) Aouani, H.; Navarro-Cia, M.; Rahmani, M.; Sidiropoulos, T. P. H.; Hong, M.; Oulton, R. F.; Maier, S. A. *Nano Lett* **2012**, *12*, 4997–5002.
- (7) Taminiau, T. H.; Moerland, R. J.; Segerink, F. B.; Kuipers, L.; van Hulst, N. F. *Nano Lett* **2007**, *7*, 28–33.
- (8) Kinkhabwala, A.; Yu, Z. F.; Fan, S. H.; Avlasevich, Y.; Mullen, K.; Moerner, W. E. *Nat. Photonics* **2009**, *3*, 654–657.
- (9) Novotny, L.; Stranick, S. J. *Annu. Rev. Phys. Chem.* **2006**, *57*, 303–331.
- (10) Catchpole, K. R.; Polman, A. *Opt Express* **2008**, *16*, 21793–21800.
- (11) Challener, W. A.; Peng, C. B.; Itagi, A. V.; Karns, D.; Peng, W.; Peng, Y. Y.; Yang, X. M.; Zhu, X. B.; Gokemeijer, N. J.; Hsia, Y. T.; Ju, G.; Rottmayer, R. E.; Seigler, M. A.; Gage, E. C. *Nat Photonics* **2009**, *3*, 220–224.
- (12) Stipe, B. C.; Strand, T. C.; Poon, C. C.; Balamane, H.; Boone, T. D.; Katine, J. A.; Li, J. L.; Rawat, V.; Nemoto, H.; Hirotsune, A.; Hellwig, O.; Ruiz, R.; Dobisz, E.; Kercher, D. S.; Robertson, N.; Albrecht, T. R.; Terris, B. D. *Nat Photonics* **2010**, *4*, 484–488.
- (13) Neubrech, F.; Pucci, A.; Cornelius, T. W.; Karim, S.; Garcia-Etxarri, A.; Aizpurua, J. *Phys. Rev. Lett.* **2008**, *101*, 157403.
- (14) Anker, J. N.; Hall, W. P.; Lyandres, O.; Shah, N. C.; Zhao, J.; Van Duyne, R. P. *Nat. Mater.* **2008**, *7*, 442–453.
- (15) Alu, A.; Engheta, N. *Phys. Rev. Lett.* **2010**, *104*, 213902.
- (16) Yu, N. F.; Genevet, P.; Kats, M. A.; Aieta, F.; Tetienne, J. P.; Capasso, F.; Gaburro, Z. *Science* **2011**, *334*, 333–337.
- (17) Genevet, P.; Yu, N. F.; Aieta, F.; Lin, J.; Kats, M. A.; Blanchard, R.; Scully, M. O.; Gaburro, Z.; Capasso, F. *Appl. Phys. Lett.* **2012**, *100*, 013101.
- (18) Aieta, F.; Genevet, P.; Yu, N. F.; Kats, M. A.; Gaburro, Z.; Capasso, F. *Nano Lett* **2012**, *12*, 1702–1706.
- (19) Xu, G.; Huang, C. M.; Tazawa, M.; Jin, P.; Chen, D. M. *J. Appl. Phys.* **2008**, *104*, 053102.
- (20) Huang, F. M.; Baumberg, J. J. *Nano Lett.* **2010**, *10*, 1787–1792.
- (21) Abb, M.; Albella, P.; Aizpurua, J.; Muskens, O. L. *Nano Lett.* **2011**, *11*, 2457–2463.
- (22) Kossyrev, P. A.; Yin, A. J.; Cloutier, S. G.; Cardimona, D. A.; Huang, D. H.; Alsing, P. M.; Xu, J. M. *Nano Lett.* **2005**, *5*, 1978–1981.
- (23) Berthelot, J.; Bouhelier, A.; Huang, C. J.; Margueritat, J.; Colas-des-Francis, G.; Finot, E.; Weeber, J. C.; Dereux, A.; Kostcheev, S.; El Ahrach, H. I.; Baudrion, A. L.; Plain, J.; Bachelot, R.; Royer, P.; Wiederrecht, G. P. *Nano Lett.* **2009**, *9*, 3914–3921.
- (24) Kim, J.; Son, H.; Cho, D. J.; Geng, B. S.; Regan, W.; Shi, S. F.; Kim, K.; Zettl, A.; Shen, Y. R.; Wang, F. *Nano Lett.* **2012**, *12*, 5598–5602.
- (25) Alu, A.; Engheta, N. *Nat. Photonics* **2008**, *2*, 307–310.
- (26) Alu, A.; Engheta, N. *Phys. Rev. Lett.* **2008**, *101*, 043901.
- (27) Schnell, M.; Garcia-Etxarri, A.; Huber, A. J.; Crozier, K.; Aizpurua, J.; Hillenbrand, R. *Nat. Photonics* **2009**, *3*, 287–291.
- (28) Liu, N.; Wen, F.; Zhao, Y.; Wang, Y.; Nordlander, P.; Halas, N. J.; Alù, A. *Nano Lett.* **2013**, *13*, 142–147.
- (29) Large, N.; Abb, M.; Aizpurua, J.; Muskens, O. L. *Nano Lett.* **2010**, *10*, 1741–1746.
- (30) Novoselov, K. S.; Geim, A. K.; Morozov, S. V.; Jiang, D.; Katsnelson, M. I.; Grigorieva, I. V.; Dubonos, S. V.; Firsov, A. A. *Nature* **2005**, *438*, 197–200.
- (31) Fei, Z.; Rodin, A. S.; Andreev, G. O.; Bao, W.; McLeod, A. S.; Wagner, M.; Zhang, L. M.; Zhao, Z.; Thieme, M.; Dominguez, G.; Fogler, M. M.; Neto, A. H. C.; Lau, C. N.; Keilmann, F.; Basov, D. N. *Nature* **2012**, *487*, 82–85.
- (32) Chen, J. N.; Badioli, M.; Alonso-Gonzalez, P.; Thongrattanasiri, S.; Huth, F.; Osmond, J.; Spasenovic, M.; Centeno, A.; Pesquera, A.; Godignon, P.; Elorza, A. Z.; Camara, N.; de Abajo, F. J. G.; Hillenbrand, R.; Koppens, F. H. L. *Nature* **2012**, *487*, 77–81.
- (33) Ju, L.; Geng, B. S.; Horng, J.; Girit, C.; Martin, M.; Hao, Z.; Bechtel, H. A.; Liang, X. G.; Zettl, A.; Shen, Y. R.; Wang, F. *Nat. Nanotechnol.* **2011**, *6*, 630–634.
- (34) Koppens, F. H. L.; Chang, D. E.; de Abajo, F. J. G. *Nano Lett.* **2011**, *11*, 3370–3377.
- (35) Yan, H. G.; Li, X. S.; Chandra, B.; Tulevski, G.; Wu, Y. Q.; Freitag, M.; Zhu, W. J.; Avouris, P.; Xia, F. N. *Nat. Nanotechnol.* **2012**, *7*, 330–334.
- (36) Yan, H. G.; Low, T.; Zhu, W. J.; Wu, Y. Q.; Freitag, M. L.; X. S.; Guinea, F.; Avouris, P.; Xia, F. N. *arXiv:1209.1984* 2012.
- (37) Emani, N. K.; Chung, T. F.; Ni, X. J.; Kildishev, A. V.; Chen, Y. P.; Boltasseva, A. *Nano Lett.* **2012**, *12*, 5202–5206.
- (38) Falkovsky, L. A.; Pershoguba, S. S. *Phys. Rev. B* **2007**, *76*, 153410.

- (39) Falkovsky, L. A.; Varlamov, A. A. *Eur. Phys. J. B* **2007**, *56*, 281–284.
- (40) Johnson, S. G.; Ibanescu, M.; Skorobogatiy, M. A.; Weisberg, O.; Joannopoulos, J. D.; Fink, Y. *Phys. Rev. E* **2002**, *65*, 066611.
- (41) Sundaramurthy, A.; Crozier, K. B.; Kino, G. S.; Fromm, D. P.; Schuck, P. J.; Moerner, W. E. *Phys. Rev. B* **2005**, *72*, 165409.
- (42) Kats, M. A.; Yu, N. F.; Genevet, P.; Gaburro, Z.; Capasso, F. *Opt. Express* **2011**, *19*, 21748–21753.
- (43) Kasry, A.; Kuroda, M. A.; Martyna, G. J.; Tulevski, G. S.; Bol, A. A. *ACS Nano* **2010**, *4*, 3839–3844.
- (44) Adam, S.; Hwang, E. H.; Galitski, V. M.; Das Sarma, S. *Proc. Natl. Acad. Sci. U.S.A.* **2007**, *104*, 18392–18397.
- (45) Weber, D.; Albella, P.; Alonso-Gonzalez, P.; Neubrech, F.; Gui, H.; Nagao, T.; Hillenbrand, R.; Aizpurua, J.; Pucci, A. *Opt. Express* **2011**, *19*, 15047–15061.
- (46) Falkovsky, L. A. *J. Phys.: Conf. Ser.* **2008**, *129*, 012004.